





## Observed Diurnal Cycles of Near-Surface Shear and Stratification in the Equatorial Atlantic and Their Wind Dependence

A. C. Hans<sup>1</sup> , P. Brandt<sup>1,2</sup> , F. Gasparin<sup>3</sup>, M. Claus<sup>1,2</sup>, S. Cravatte<sup>3,4</sup> , J. Horstmann<sup>5</sup>, and G. Reverdin<sup>6</sup> 

<sup>1</sup>GEOMAR Helmholtz Centre for Ocean Research Kiel, Kiel, Germany, <sup>2</sup>Faculty of Mathematics and Natural Sciences, Kiel University, Kiel, Germany, <sup>3</sup>Université de Toulouse, LEGOS (IRD/UT3/CNES/CNRS), Toulouse, France, <sup>4</sup>IRD Centre, Nouméa, New Caledonia, <sup>5</sup>Helmholtz Centre Hereon, Radar Hydrography, Geesthacht, Germany, <sup>6</sup>Sorbonne Université - CNRS - IRD - MNHN, Laboratoire LOCEAN - IPSL, Paris, France

### Key Points:

- Basin-scale in-situ data show the evolution of diurnal warm layer and diurnal jet in the upper 15 m of the equatorial Atlantic Ocean
- Higher wind speeds lead to earlier diurnal peaks, deeper penetration depths, and faster descent rates of the diurnal jet
- Wind speed dependence of descent rates of diurnal shear and stratification can explain the varying onset of deep-cycle turbulence

### Supporting Information:

Supporting Information may be found in the online version of this article.

### Correspondence to:

A. C. Hans,  
ahans@geomar.de

### Citation:

Hans, A. C., Brandt, P., Gasparin, F., Claus, M., Cravatte, S., Horstmann, J., & Reverdin, G. (2024). Observed diurnal cycles of near-surface shear and stratification in the equatorial Atlantic and their wind dependence. *Journal of Geophysical Research: Oceans*, 129, e2023JC020870. <https://doi.org/10.1029/2023JC020870>

Received 29 DEC 2023

Accepted 27 JUL 2024

### Author Contributions:

**Conceptualization:** A. C. Hans, P. Brandt

**Formal analysis:** A. C. Hans

**Funding acquisition:** P. Brandt,

F. Gasparin

**Investigation:** A. C. Hans

**Supervision:** P. Brandt, F. Gasparin,

M. Claus

**Visualization:** A. C. Hans

**Writing – original draft:** A. C. Hans

**Writing – review & editing:** A. C. Hans,

P. Brandt, F. Gasparin, M. Claus,

S. Cravatte, J. Horstmann, G. Reverdin

**Abstract** The diurnal cycles of near-surface velocity and temperature, also known as diurnal jet and diurnal warm layer (DWL), are ubiquitous in the tropical oceans, affecting the heat and momentum budget of the ocean surface layer, air-sea interactions, and vertical mixing. Here, we analyze the presence and descent of near-surface diurnal shear and stratification in the upper 20 m of the equatorial Atlantic as a function of wind speed using ocean current velocity and hydrographic data taken during two trans-Atlantic cruises along the equator in October 2019 and May 2022, data from three types of surface drifters, and data from Prediction and Research Moored Array in the Tropical Atlantic (PIRATA) moorings along the equator. The observations during two seasons with similar mean wind speeds but varying surface heat fluxes reveal similar diurnal jets with an amplitude of about  $0.11 \text{ m s}^{-1}$  and similar DWLs when averaging along the equator. We find that higher wind speeds lead to earlier diurnal peaks, deeper penetration depths, and faster descent rates of DWL and diurnal jet. While the diurnal amplitude of stratification is maximum for minimal wind speeds, the diurnal amplitude of shear is maximum at 6 m depth for moderate wind speeds of about  $5 \text{ m s}^{-1}$ . The inferred wind dependence of the descent rates of DWL and diurnal jet is consistent with the earlier onset of deep-cycle turbulence for higher wind speeds. The DWL and the diurnal jet not only trigger deep-cycle turbulence but are also observed to modify the wind power input and thus the amount of energy available for mixing.

**Plain Language Summary** During daytime, solar radiation leads to the formation of a thin warm layer at the ocean surface which can trap heat and wind-forced momentum. Both heat and momentum are transported in the deeper ocean during the evening and night by turbulent mixing. The associated diurnal variation of temperature, current velocity, and their vertical gradients, stratification and velocity shear, are thus relevant for understanding ocean-atmosphere interactions. This study investigates how the diurnal variation in stratification and velocity shear is influenced by the wind speed. For that, basin-scale observations of velocity and temperature, which were collected in the equatorial Atlantic during two trans-Atlantic equatorial cruises and by instruments installed at long-term moorings along the equator, are analyzed. These observations reveal that the wind speed influences the amplitude, the timing, and the vertical structure of the diurnal variation in stratification and velocity shear. Wind speed also influences how deep and how fast this variation propagates from the surface downward. The study concludes that the diurnal variation of stratification and velocity shear impacts first the input of mechanical energy from the atmosphere into the ocean and second the process of turbulent mixing below the night-time mixed layer.

## 1. Introduction

Oceanic parameters such as stratification, shear, and mixing vary close to the ocean surface with the diurnal cycle of solar radiation. After sunrise, solar radiation is absorbed by the ocean which leads to a warming of the ocean surface with the ocean absorption decreasing exponentially with depth (e.g., Delnore, 1972; Gentemann et al., 2009; Soloviev & Lukas, 1997). The difference in the heat input depending on depth leads to the formation of a so-called diurnal warm layer (DWL) which slides over the water below with minimal friction (“slippery” layer). Heat and wind-forced momentum are trapped close to the surface, creating a highly-sheared near-surface diurnal jet. The stratified shear layer descends during late afternoon and evening, transporting heat and momentum downward into the deeper ocean. After sunset, cooling of the sea surface and convective overturning

© 2024. The Author(s).

This is an open access article under the terms of the [Creative Commons Attribution License](https://creativecommons.org/licenses/by/4.0/), which permits use, distribution and reproduction in any medium, provided the original work is properly cited.

destroy the DWL (e.g., Kudryavtsev & Soloviev, 1990; Price et al., 1986; Smyth et al., 2013; Soloviev & Lukas, 2014; Woods & Strass, 1986). This diurnal variability of temperature and velocities and consequently shear and stratification is linked to diurnal variability of turbulent dissipation both within the DWL (Soloviev & Lukas, 2014; St. Laurent & Merrifield, 2017; Sutherland et al., 2016) and below (Moum et al., 2022; Peters et al., 1988). Therefore, the near-surface diurnal cycle modifies near-surface heat and momentum budgets and plays a role in air-sea interactions and vertical mixing.

Understanding the near-surface diurnal cycle of the ocean is of particular interest in equatorial regions for several reasons:

1. The equatorial Atlantic and Pacific are characterized by zonal current systems and a highly-sheared Equatorial Undercurrent (EUC), eventually leading to the presence of marginal instability. Marginal instability is defined as a state in which shear and stratification vary almost proportionally so that the Richardson number remains close to its critical value (Smyth et al., 2019; Smyth & Moum, 2013). In the equatorial Pacific it is observed that, when the descending diurnal shear layer merges with the marginally unstable shear above the EUC core, shear instabilities are induced that can trigger turbulence, the so-called deep-cycle turbulence (DCT) (Pham et al., 2013; Smyth et al., 2013; Smyth & Moum, 2013). DCT also occurs in the equatorial Atlantic, but it is still an open question whether there are fundamental differences in the nature of instabilities leading to DCT in the Atlantic and Pacific (Moum et al., 2023).
2. DWL and associated diurnal jet are observed to reach and thus impact the ocean far deeper near the equator than away from it (Masich et al., 2021). This discrepancy arises due to a combination of Coriolis rotational effects that are vanishing toward the equator disabling the rotation of horizontal velocities with depth (Hughes et al., 2020a) and the presence of very high background shear and marginal instability near the equator supporting the descent of the shear layer (e.g., Lien et al., 1995; Masich et al., 2021).
3. Equatorial cold tongue regions are critical for the global heat balance and the near-surface diurnal cycle presents a key mechanism there for the heat transfer from the atmosphere to the stratified ocean below the surface mixed layer (Moum et al., 2013; Whitt et al., 2022). Upwelling and mixing in these regions define not only the downward heat flux but similarly the upward nitrate flux (Brandt et al., 2023; Radenac et al., 2020), stressing the importance of diurnal variability at the equator also for biological productivity.

The prevailing atmospheric forcing and in particular the wind speed are known to influence the formation and the structure of the DWL and the associated diurnal jet as indicated by observational (Hughes et al., 2020b; Masich et al., 2021; Soloviev & Lukas, 1997; Wenegrat & McPhaden, 2015) and modeling studies (Gentemann et al., 2009; Hughes et al., 2020a, 2021), where the diurnal cycle of the wind itself can be neglected as it is at least one order of magnitude smaller than the daily-mean wind signal magnitude (Masich et al., 2021; Smyth et al., 2013). Yet, there does not seem to be a clear consensus emerging from previous studies. It has been suggested for equatorial to subtropical regions that DWLs and diurnal jets do not exist for wind speeds exceeding a threshold ranging between  $6 \text{ m s}^{-1}$  and  $8 \text{ m s}^{-1}$  (Hughes et al., 2021; Kudryavtsev & Soloviev, 1990; Matthews et al., 2014; Thompson et al., 2019). However, it should be noted that pronounced DWL, diurnal jet, and DCT have been observed for wind speeds at about  $8 \text{ m s}^{-1}$  (Masich et al., 2021; Moum et al., 2023; Smyth et al., 2013). In the equatorial Atlantic, Wenegrat and McPhaden (2015) observed a seasonal variability with pronounced descending diurnal shear layers and limited diurnal sea surface temperature variability in steady trade wind conditions during boreal summer and autumn, and opposite patterns in weak wind conditions during boreal winter and spring. More comprehensive analyses of the interaction between the wind and DWL and diurnal jet have been performed in the tropical Pacific. For higher wind speeds, the penetration depth of the DWL and the associated diurnal jet becomes deeper (Hughes et al., 2020b; Masich et al., 2021; Price et al., 1986), consistent with Wenegrat and McPhaden (2015) results, and the descent rate of the DWL increases (Hughes et al., 2020b). For the diurnal jet amplitude, Price et al. (1986) suggested based on a simple mixed-layer model that it is solely dependent on the net surface heat flux and consequently independent of the wind speed. In contrast, Masich et al. (2021) found a positive linear relationship between the wind speed and the strength of the diurnal jet at equatorial sites where marginal instability was present. By applying an idealized model, Hughes et al. (2020a) also showed a dependence of the maximum shear within the DWL on the wind speed but instead with the maximum shear being reached for wind speeds of  $2 \text{ m s}^{-1}$ . Hence, there is a lack of a comprehensive understanding of the interplay between wind and diurnal jet regarding descent rates and diurnal amplitudes as well as a lack of a confirmation of the processes observed in the tropical Pacific for the tropical Atlantic.

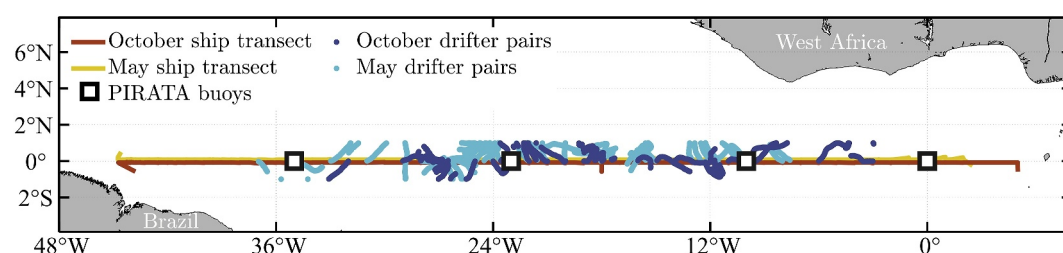


**Figure 1.** Geographical map of the observations used in the present study. Displayed are the equatorial transects of the October 2019 (red line) and May 2022 (yellow line) TRATLEQ cruises, mean positions of drifter pairs within 1° north and south of the equator deployed during the TRATLEQ cruises in October (dark blue dots) and May (light blue dots), and the locations of the PIRATA buoys (black-bordered squares).

In addition to the DWL, there is a cool-skin layer in the upper few millimeters of the ocean, which is a thermally stratified layer resulting from the ocean heat loss to the atmosphere. This layer is also subject to diurnal variations but usually exists both day and night as well as under strong wind conditions (e.g., Donlon et al., 2002; Gentemann & Minnett, 2008; Kawai & Wada, 2007; Ward, 2006). Note that this study neglects processes shallower than 1 m depth and thus neglects the cool-skin layer.

While numerous satellite and in-situ measurements of diurnal temperature variations exist close to the surface (e.g., Delnore, 1972; Gentemann et al., 2009; Kawai et al., 2006; Kawai & Wada, 2007; Soloviev & Lukas, 1997; Ward, 2006), observations of ocean currents close to the surface and thus also observations of the diurnal jet are still rare due to measurement constraints and noise. For example, shipboard measurements with acoustic Doppler current profilers (ADCP) typically cover a depth range below 15 m depth and shallow moored measurements with upward looking ADCPs are contaminated by interference with surface reflections or aggregation of fish (Elipot & Wenegrat, 2021; Röhrs et al., 2021). However, near-surface estimates within the upper 10 m are necessary to properly capture the diurnal dynamics. Only few studies provide observational estimates within the upper 10 m at diurnal time scales. These studies are located in the tropics to subtropics and are based on different types of surface drifters (Kudryavtsev & Soloviev, 1990), on current meters and/or ADCPs attached to moorings and surface buoys (Cronin & Kessler, 2009; Pham et al., 2017; Price et al., 1986; Sutherland et al., 2016; Wenegrat & McPhaden, 2015), or to surface-following platforms, such as the SurfOtter (Hughes et al., 2020a). The resulting diurnal jet amplitudes vary from  $10 \text{ cm s}^{-1}$  to  $20 \text{ cm s}^{-1}$  with different associated depth intervals, different locations as well as different seasons and prevailing background conditions. The vertical structure of near-surface shear and factors influencing the diurnal jet are still poorly understood.

This study combines observational data sets from the TRATLEQ cruises, which are two trans-Atlantic equatorial cruises with dedicated en-route measurements and associated drifter deployments, and data sets from specially-instrumented Prediction and Research Moored Array in the Tropical Atlantic (PIRATA) moorings to capture diurnal stratification and shear in the upper 15 m of the equatorial Atlantic Ocean. With these data sets, we aim to assess near-surface diurnal dynamics focusing on the influence of background conditions and, in particular, on the wind speed dependency. The study addresses the lack of near-surface measurements and the knowledge deficit about the wind dependency of the diurnal jet and the DWL in the equatorial Atlantic. The paper is organized as follows. Data and methodology are described in Sections 2 and 3, respectively. Results about the near-surface diurnal cycle in the equatorial Atlantic and impacts of different background conditions are presented in Section 4. The impact of the wind speed on diurnal shear and stratification is examined in more detail in Section 5. The results are then discussed in terms of descent rates of diurnal shear and stratification and are linked to the wind dependence of DCT found by Moum et al. (2023) in Section 6.2. The impact of the described diurnal cycles on the wind power input (WPI) is discussed in Section 6.3.

## 2. Observational Data

This study focuses on different observational data sets from the TRATLEQ expeditions, consisting of two research cruises and associated surface drifter experiments, and data sets from PIRATA moorings (Figure 1).

## 2.1. TRATLEQ Cruises

Shipboard measurements were carried out during the cruises M158 and M181 with the research vessel Meteor, the so-called TRATLEQ (TRAns-ATLantic EQuatorial) cruises I and II. The cruises provide equatorial Atlantic transects from 5°E to 45°W between 29 September and 22 October 2019 and from 2°E to 45°W between 30 April and 20 May 2022. In the following, the TRATLEQ I cruise will be termed October transect and the TRATLEQ II cruise May transect.

For both cruises, near-surface stratification is estimated from 10 s temperature and salinity measurements by the ship's dual thermosalinograph (TSG) as well as 10 s pitch and roll data from the ship's motion reference unit (more details in Section 3.2). The vessel measures the speed and direction of the wind at 35 m height as well as global short-wave radiation (SWR) with a temporal resolution of 1 min.

Direct shipboard velocity measurements conducted with a marine radar and a vessel-mounted ADCP (vmADCP) are considered for the October transect. A coherent-on-receive marine X-band (9.4 GHz) radar developed at the Helmholtz Centre Hereon (Horstmann et al., 2021) was installed. The instrument was set to operate at a pulse length of 50 ns (i.e., short-pulse mode), providing a range resolution of 7.5 m. It is equipped with a vertical transmit and receive (VV) polarized antenna of 2.3 m (7.5 ft) with a beam width of 1.1°, a rotational period of 2 s and a pulse repetition frequency of 2 kHz. The obtained image sequences are analyzed with respect to the surface wave properties such as wave directions, wave lengths, and phase velocities. The surface current vector is then resulting from the difference between the observed phase velocities and the phase velocities given by the linear dispersion relation of surface gravity waves (Horstmann et al., 2015; Lund et al., 2018). The retrieved surface current layer varies between 1 m and 5 m depth, depending on the surface wave length. Here, a mean depth of 3 m is assumed for the marine radar measurements. A validation study in the Gulf of Mexico showed a root-mean-square error of 4 cm s<sup>-1</sup> compared to velocities of surface drifters representing the upper 0.4 m depth (Lund et al., 2018). In addition to the marine radar, a vmADCP, a 75 kHz RDI Ocean Surveyor, was installed with the bin size set to 8 m (Brandt et al., 2022). Here, only data from the uppermost bin centered at 17 m depth are considered. Hourly velocity data from the vmADCP have an accuracy of 1 cm s<sup>-1</sup> for on-station and 2–4 cm s<sup>-1</sup> for underway measurements varying with wave and wind conditions (J. Fischer et al., 2003). For the May transect, no direct shipboard velocity measurements are considered as a different vmADCP with a reduced signal-to-noise ratio for the uppermost bin was installed, leading to a distortion of the diurnal cycle.

## 2.2. TRATLEQ Drifter Experiments

During both TRATLEQ cruises, drifter experiments were carried out that consisted of pairwise deployments of two types of surface drifters about every 1° longitude along the equator. During the October transect, 26 SVP (Surface Velocity Program) drifters, drifting with velocities at about 15 m depth, and 27 CARTHE (Consortium for Advanced Research on Transport of Hydrocarbon in the Environment) drifters, providing velocities at about 0.5 m depth, were deployed between 29 September and 18 October 2019. During the May transect, 18 SVP drifters and 44 Hereon drifters, which are similar to CARTHE drifters and provide velocities at about 0.5 m depth, were deployed between 04 May and 17 May 2022. Both trajectory data sets were quality-controlled and interpolated to hourly values. Estimates of the velocity difference between 0.5 m and 15 m were then based on drifter pairs that are separated in time by less than 1 hr and in distance by less than 100 km (details in Text S1 and Figures S1 and S2 in Supporting Information S1). This study considers 6,589 drifter pairs between 02 October and 29 October 2019 in the area from 33°W to 3°W and 1°S to 1°N as well as 9,602 drifter pairs between 04 May and 02 June 2022 in the area from 37°W to 8°W and 1°S to 1°N. The mean distance between the paired drifters is 46 km for the October drifter experiment and 54 km for the May drifter experiment.

## 2.3. PIRATA Moorings

We use data from equatorial surface buoys of the PIRATA (Prediction and Research Moored Array in the Tropical Atlantic) moorings providing wind speed and direction at 4 m height and SWR, long-wave radiation, latent, and sensible heat fluxes. Below the surface, we consider data from temperature and conductivity measured at 1 m, 5 m, 10 m, 20 m, and 40 m depth. In particular, we use wind data from the equatorial PIRATA sites at 0°W, 10°W, 23°W, and 35°W for the whole available period between 1999 and 2022 (Bourlès et al., 2019). Near-surface temperature and conductivity data are considered over the same period at 10°W and 23°W (Bourlès et al., 2019). Heat fluxes estimates at 10°W and 23°W provided by ePIRATA are used for the periods of the May

and October transects and drifter experiments (Foltz et al., 2018). Additionally, we use data from a Teledyne-RDI Sentinel Workhorse 600 kHz ADCP which was deployed at 0°N, 23°W from 13 October 2008 until 18 June 2009, providing hourly velocity averages from a depth of 4.3–38.8 m (see Wenegrat et al., 2014). The data set is masked according to ([https://www.pmel.noaa.gov/tao/drupal/disdel/adcp\\_0n23w/index.html](https://www.pmel.noaa.gov/tao/drupal/disdel/adcp_0n23w/index.html)). This period of near-surface moored velocity measurements with high vertical resolution will be referred to as enhanced monitoring period (EMP).

## 2.4. Satellite Wind Data

Winds at 10 m height are taken from the gridded 6-hourly Cross-Calibrated Multi-Platform (CCMP) near-real time wind satellite product provided by Remote Sensing Systems for the period January 2000 to November 2022. The product is used to estimate the wind at the drifter locations. The CCMP V2.0 product is processed to L3 standard, has a horizontal resolution of  $0.25^\circ \times 0.25^\circ$  and a temporal resolution of 6 hr (Atlas et al., 2011). Averages to daily mean zonal and meridional wind components are considered for the following analysis because the diurnal warming is a cumulative process which depends on the history of heat and momentum fluxes during the hours after sunrise.

## 3. Methods

### 3.1. Stratification From the PIRATA Moorings

For the PIRATA moorings, the stratification,  $N^2$ , is given as squared Brunt-Väisälä frequency and can be calculated according to IOC et al. (2010) as

$$N^2 = g^2 \cdot \rho \cdot \frac{\beta \cdot \Delta S_A - \alpha \cdot \Delta \theta}{\Delta P} \quad (1)$$

where  $\Delta \theta$  is the conservative temperature difference,  $\Delta S_A$  the absolute salinity difference, and  $\Delta P$  the corresponding pressure difference,  $\rho$  the in-situ density,  $g$  the gravitational acceleration, and  $\alpha$  and  $\beta$  the coefficients of thermal expansion and saline contraction, respectively. The respective parameters are computed using the Gibbs SeaWater Oceanographic Toolbox of TEOS-10.

### 3.2. Stratification From the Vessel-Mounted Thermosalinograph

The stratification,  $N^2$ , at the depth of the TSG inlet can be estimated using data taken at a high sampling rate (here  $0.1 \text{ s}^{-1}$ ) for temperature, salinity, and the vertical movement of the inlet position relative to the water column. This method was first described in T. Fischer et al. (2019). The vertical distance of the inlet relative to the ship's center of mass is evaluated as

$$d' = (Y \cdot \sin(\psi) - Z \cdot \cos(\psi)) \cdot \cos(\gamma) - X \cdot \sin(\gamma) \quad (2)$$

where  $(X, Y, Z)$  is the inlet position relative to the center of mass in ship's coordinates, positive for (bow, starboard, up). For the RV Meteor III,  $(X, Y, Z) = (40 \text{ m}, -3 \text{ m}, -2 \text{ m})$ . Moreover,  $\psi$  is the roll angle positive for starboard down, and  $\gamma$  is the pitch angle positive for bow up. With the ship's center of mass being 1 m below sea level, the mean depth of the inlet below sea level is  $4.1 \text{ m} \pm 0.4 \text{ m}$  during the October transect and  $4.0 \text{ m} \pm 0.4 \text{ m}$  during the May transect. Neglecting  $\Delta S_A$  in Equation 1 and using the hydrostatic approximation,  $N^2$  at the inlet position can be estimated as

$$N^2 \approx g \cdot \alpha \cdot T_z \text{ with } T_z = \frac{\sqrt{\text{var}(T)}}{\sqrt{\text{var}(d')}} \quad (3)$$

where  $T_z$  is the vertical temperature gradient and  $T$  is the temperature measured at the TSG inlet. This calculation does not consider surface waves (see T. Fischer et al. (2019) for more details) and the actual flow along the ship's hull which causes uncertainties in the actual depth of the sampled water and in the measured properties.

Consequently, the derived  $N^2$  time series is not analyzed quantitatively, but is used qualitatively to detect temporal variations in near-surface stratification.

### 3.3. Vertical Shear of Horizontal Velocities

Four different velocity data sets are considered in this study: (1). Marine radar and vmADCP data for the October transect, (2). CARTHE and SVP drifter positions for the October drifter experiment, (3). Hereon and SVP drifter positions for the May drifter experiment, and (4). EMP data at the PIRATA site  $0^\circ\text{N}$ ,  $23^\circ\text{W}$ . For all four data sets, the zonal and meridional ocean velocities are transformed into an along- and across-wind coordinate system. This transformation allows an easier identification of the diurnal jet as, according to its definition, the jet is created by wind momentum that is trapped in the DWL. A positive across-wind component corresponds to velocities to the left of the wind direction. The chosen wind value (satellite winds for data sets 1–3, PIRATA winds for data set 4) is the daily-mean value that is closest in time and space to the velocity measurements. The vertical shear of horizontal velocities in along-wind direction,  $Sh_{A1}$ , is defined as the vertical derivative of the along-wind velocities.

### 3.4. Diurnal Cycle Diagnostics

Mean diurnal cycles are created by taking the mean of hourly bins. The uncertainty associated with the hourly means is quantified by the standard error which is computed as the standard deviation divided by the square root of the degrees of freedom with the assumption of one independent value per day. The time is considered in Local Solar Time (LST) so that solar noon is centered at 12:00, using a conversion by Koblick (2021).

Diurnal patterns are compared in terms of the diurnal timing and the diurnal amplitude. The peak timing and value are determined by a sinusoidal fit  $f(t) = \alpha \cdot \sin(\omega \cdot t + \varphi)$  as a function of time  $t$  [days] considering  $\pm 3.5$  hr around the maxima of the hourly means (i.e., 7 values of the hourly time series are used). Only periods ( $\frac{2-\pi}{\omega}$ ) between 0.5 and 2 days and phases ( $\varphi$ ) smaller than 1 day are considered. A symmetric fit is assumed to be a good enough approximation, though there might be a tendency for a slower increase and a faster decrease. The amplitude is calculated as the difference of the peak value determined by the fit and the minimum of the hourly means between 6:00 LST (sun rise) and the peak time. These two characteristics are calculated for all robust diurnal cycles where the robustness is determined using a signal-to-noise ratio. The signal is defined as the amplitude, and the noise is defined as the arithmetic mean of the hourly computed standard errors. If the signal-to-noise ratio exceeds 2.5 for  $Sh_{A1}$  and 10 for  $N^2$ , we assume the presence of a robust diurnal cycle for  $Sh_{A1}$  and  $N^2$  as well as the presence of a DWL and a diurnal jet, respectively. In order to determine the accuracy of the sinusoidal fits, the bootstrapping method is utilized. This method provides confidence intervals (CI) for the estimated parameters without prior knowledge of the shape of the underlying distribution (Efron, 1979). For each diurnal fit, 10,000 resamples are taken from the original data set with replacement and the same probability for each datapoint to be selected. Each set of resamples has the sample size of the original data set. From the resulting distribution of parameters for the diurnal fit, a 95% CI is given by taking the 2.5% and 97.5% quantiles.

### 3.5. Wind Speed, Wind Stress, and Wind Power Input

For comparability, mean wind speeds are calculated from zonal and meridional components at daily resolution. The shipboard wind measurements from the TRATLEQ cruises taken at 35 m height and the PIRATA buoy wind measurements taken at 4 m height are scaled to 10 m wind velocities using a logarithmic wind profile for neutral conditions. For a given height,  $z$ , the 10 m winds can be calculated as

$$W(10\text{ m}) = W(z) \cdot \frac{\ln(10\text{ m}) - \ln(z_0)}{\ln(z) - \ln(z_0)} \quad (4)$$

where  $W$  is the wind velocity and  $z_0$  the surface roughness length (Fleagle & Businger, 1980) with offshore assuming  $z_0 = 0.0002$  (Dutton, 1995). In the following, the horizontal wind vector at 10 m height is denoted as  $\mathbf{u}_{10}$ . The wind stress vector,  $\boldsymbol{\tau}$ , is then defined as (Pacanowski, 1987)

$$\boldsymbol{\tau} = \rho_a \cdot c_D \cdot (\mathbf{u}_{10} - \mathbf{u}) \cdot |\mathbf{u}_{10} - \mathbf{u}| \quad (5)$$

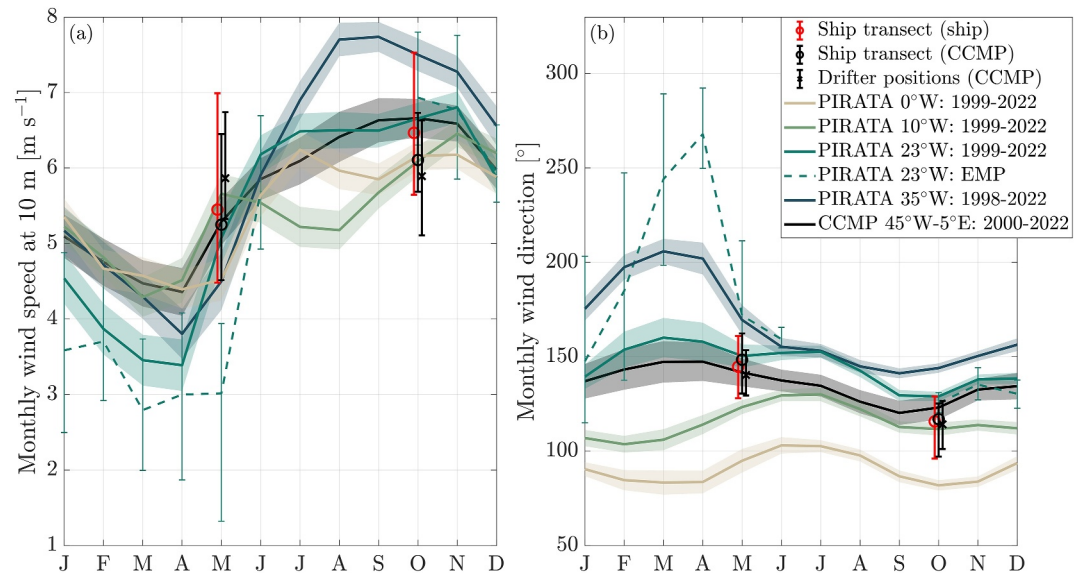


**Figure 2.** Seasonal wind climatologies for the equatorial Atlantic and wind conditions during measurement campaigns. Mean seasonal (a) wind speed at 10 m height calculated from daily mean wind speeds and (b) wind direction in polar coordinates ( $0^\circ$  corresponds to westerlies,  $90^\circ$  to southerlies) derived from wind measurements at four different PIRATA sites (colored lines) and from CCMP winds (black lines) at the equator. The dashed line corresponds to PIRATA winds measured at  $0^\circ\text{N}$ ,  $23^\circ\text{W}$  during the EMP (from October 2008 until June 2009). Values for the TRATLEQ expeditions are derived from the ship's sensors along the ship transects (red circle) and by interpolating CCMP winds on the drifter (black cross) and ship positions (black circle). Shading denotes  $\pm$  one standard error of the monthly mean assuming one independent value per month, and error bars denote the interquartile range.

where  $\rho_a = 1.223 \text{ kg m}^{-3}$  is the density of air,  $c_D = 0.0013$  the drag coefficient, and  $\mathbf{u}$  the observed ocean surface velocity vector.

The WPI is the mechanical energy transferred by winds into the ocean. Part of this energy drives upper-ocean turbulence and is locally dissipated (Moum & Caldwell, 1985). The wind stress works on the ocean flow, so that the WPI is defined as

$$\text{WPI} = \boldsymbol{\tau} \cdot \mathbf{u} \cdot \rho_w^{-1} \quad (6)$$

where  $\rho_w = 1025 \text{ kg m}^{-3}$  is the density of sea water. Note that ignoring the effect of the ocean surface velocity on  $\boldsymbol{\tau}$ , that is, using  $\mathbf{u}_{10}$  instead of the velocity difference  $(\mathbf{u}_{10} - \mathbf{u})$  in Equation 5, leads to a 3%/5%/16% increase in the mean  $\boldsymbol{\tau}$  if  $\mathbf{u}$  were velocities at 0.5 m depth from the CARTHE drifters/velocities at 0.5 m depth from the Hereon drifters/velocities at 4.3 m depth of the EMP at  $0^\circ\text{N}$ ,  $23^\circ\text{W}$ . This increase is derived using daily-mean wind speeds and hourly ocean velocities.

## 4. Diurnal Cycle in the Equatorial Atlantic Across the Basin

### 4.1. Background Conditions

Given that wind and net surface heat flux are assumed to potentially govern the pattern of the diurnal cycles of near-surface shear and stratification, we start by investigating these two atmospheric fields as background conditions to classify diurnal shear and stratification obtained during the two TRATLEQ ship transects and drifter experiments.

Monthly climatologies of wind speed and direction in the equatorial Atlantic are derived from PIRATA buoys at four different longitudes and from the CCMP product zonally averaged between  $45^\circ\text{W}$  and  $5^\circ\text{E}$ , using the available time series (Figure 2). The CCMP winds have a seasonal cycle with a minimum speed of  $4.4 \text{ m s}^{-1}$  in April and a maximum speed of  $6.7 \text{ m s}^{-1}$  in October associated with the meridional migration of the Intertropical Convergence Zone (Waliser & Gautier, 1993). The wind is directed toward the northwest, ranging from  $120^\circ$

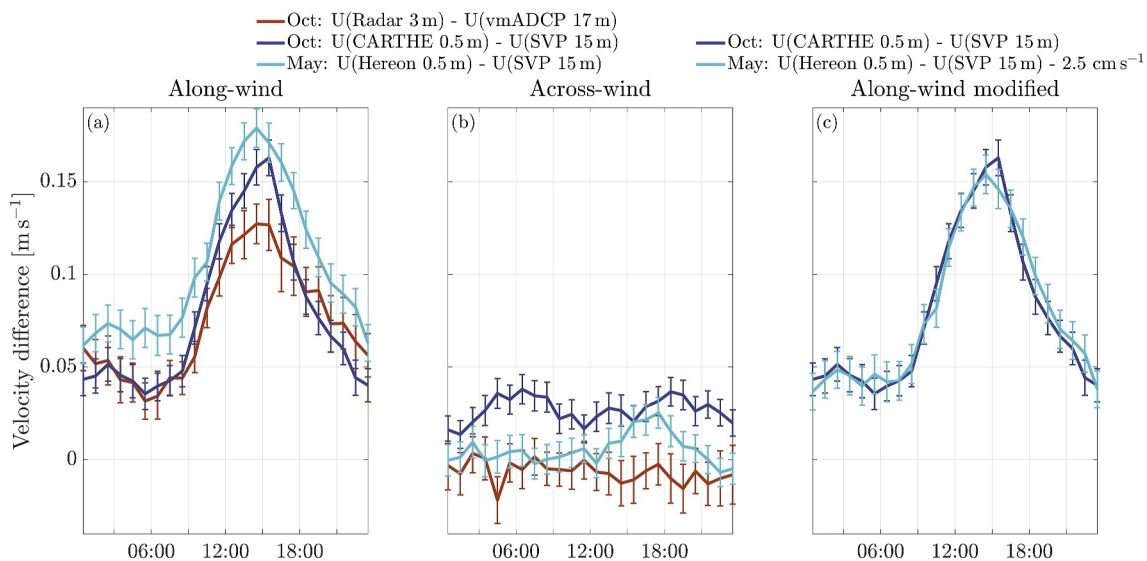


**Figure 3.** Mean diurnal cycles of vertical differences of horizontal velocities in (a) along- and (b) across-wind direction as a function of LST. The velocity differences are obtained from the marine radar and the uppermost bin of the vmADCP during the October transect (dark red) and from the October (dark blue) and May (light blue) drifter experiments. Further, (c) compares the drifter experiments in (a) with a background velocity difference of  $2.5 \text{ cm s}^{-1}$  removed for the May experiment. The error bars represent the standard error.

(SSE) in September to  $148^\circ$  (SE) in March. CCMP winds along the equator are mostly consistent with PIRATA measurements at  $23^\circ\text{W}$  and  $10^\circ\text{W}$ . The PIRATA measurements further indicate that whilst the amplitude of seasonal variations in wind speed and direction is decreasing from the western to the eastern basin, the prevailing wind direction is changing from easterlies to southerlies across the basin.

This seasonal wind variability is the main reason for the different wind conditions that prevail during the two ship transects and drifter experiments in October 2019 and May 2022, shown as zonal means in Figure 2. The mean wind speed differed by  $0.9 \text{ m s}^{-1}$  and  $1.0 \text{ m s}^{-1}$  for the two ship transects considering CCMP winds and ship's sensor winds, respectively. The mean wind speed at the location of the drifter pairs is the same for the two experiments. There were similar wind conditions for the transect and associated drifter experiment in October and an offset of  $0.6 \text{ m s}^{-1}$  in May. The mean wind direction changed by about  $30^\circ$  between the two transects and between the two drifter experiments, yielding more northward (meridional) winds in October and more westward (zonal) winds in May. A comparison of the wind conditions during the two transects and drifter experiments with the zonal mean CCMP climatology suggests that the observed wind direction was typical and the wind speed atypical with respect to the climatological seasonal cycle (Figure 2).

The net surface heat flux is computed as the sum of SWR, long-wave radiation, latent, and sensible heat flux. While the mean SWR differs only by  $14 \text{ W m}^{-2}$  between the two transects, there is a larger difference between the drifter experiments. Averaging the SWR measured at the PIRATA buoys at  $0^\circ\text{N}$ ,  $10^\circ\text{W}$  and  $0^\circ\text{N}$ ,  $23^\circ\text{W}$  for the periods of the two drifter experiments yields  $31 \text{ W m}^{-2}$  (14%) higher SWR during the October compared to the May experiment. The net surface heat flux is higher by  $39 \text{ W m}^{-2}$  (45%) respectively.

Hence, the two periods are characterized by a comparable mean wind speed for the May and October drifter experiments, while the mean wind speed is about  $1 \text{ m s}^{-1}$  smaller for the May compared to the October ship transect. The mean wind direction is shifted by about  $30^\circ$  comparing both the two drifter experiments and the two transects (Figure 2). Furthermore, the net surface heat flux is noticeably weaker and the SWR slightly weaker for the May compared to the October drifter experiment.

#### 4.2. Observed Near-Surface Diurnal Shear

The mean diurnal cycles of vertical differences of horizontal velocities are investigated that were measured between 0.5 m and 15 m depth by CARTHE/Hereon and SVP drifters and between 3 and 17 m depth by the marine radar and the vmADCP (Figure 3). For all data sets, there are stronger diurnal and background signals in



**Table 1**

*Background Conditions in the Western, Central, and Eastern Equatorial Atlantic Basin During the October and May Drifter Experiments*

October experiment	Western: 37°W to 25°W	Central: 25°W to 17°W	Eastern: 17°W to 3°W
May experiment			
Wind speed [ $\text{m s}^{-1}$ ], wind direction [ $^{\circ}$ ]	$6.0 \pm 0.8, 129 \pm 15$	$6.0 \pm 0.7, 116 \pm 13$	$5.7 \pm 1.1, 99 \pm 18$
	$6.1 \pm 0.8, 158 \pm 14$	$5.5 \pm 1.2, 135 \pm 32$	$6.0 \pm 1.0, 127 \pm 16$
Diurnal amplitude of along-wind velocity differences [ $\text{cm s}^{-1}$ ]	13.5	13.2	14.6
	12.0	12.9	13.8
0–6 LST mean velocity difference along-wind (zonal, meridional) [ $\text{cm s}^{-1}$ ]	$4.6 \pm 1.7 (-8.0 \pm 1.5, -0.7 \pm 1.6)$	$3.9 \pm 1.6 (-0.3 \pm 1.4, 4.8 \pm 1.6)$	$4.6 \pm 1.2 (-4.0 \pm 1.3, 2.4 \pm 1.1)$
	$8.4 \pm 2.2 (-9.2 \pm 2.1, -0.1 \pm 1.2)$	$1.2 \pm 1.5 (-2.2 \pm 1.7, 0.4 \pm 1.7)$	$11.8 \pm 1.4 (-9.2 \pm 1.6, 7.3 \pm 1.0)$

*Note.* The mean CCMP wind speed and direction as well as the diurnal amplitude and the night-time (0:00 to 6:00 LST) mean of the along-wind velocity differences between 0.5 and 15 m depth are calculated for three longitudinal groups. For the night-time mean velocity difference, the zonal and meridional components are additionally given in brackets.

the along-wind component than in the across-wind component (Figures 3a and 3b), implying that the vertical differences of near-surface velocities are mainly wind driven. Therefore, only the along-wind component is considered in the following. A clear diurnal cycle is seen in the along-wind velocity differences (Figure 3a). Velocity differences are at their minimum in the morning hours (from 0:00 to 6:00 LST), increase after sunrise (6:00 LST) until they reach their maximum between 14:00 and 16:00 LST (2–4 hr after solar noon) and decrease in the evening - corresponding to the daytime formation of a diurnal jet. This results in diurnal amplitudes of  $12.7 \text{ cm s}^{-1}$  (October drifter experiment),  $9.6 \text{ cm s}^{-1}$  (October ship transect), and  $11.7 \text{ cm s}^{-1}$  (May drifter experiment). Note that the derived diurnal amplitudes can be regarded as diurnal jet amplitudes as there is no robust diurnal signal in the mean drifter velocities at 15 m depth. The diurnal amplitude obtained from the October drifter experiment exceeds the one from the October ship transect by 32% while the night-time velocity differences are the same. Overall, the two measurement techniques are in good agreement, showing the robustness of the diurnal cycle and giving confidence in the usage of both techniques. The distance criterion of 100 km used for the collocation of pairs of the two drifter types reveals that the diurnal cycle is also a horizontally large-scale feature, matching previous findings (Bellenger & Duvel, 2009).

The two drifter experiments yield closely resembling diurnal cycles for the vertical differences of horizontal velocities between 0.5 m and 15 m depth (Figure 3c). While the pattern of the diurnal cycles agrees well, there is an offset of about  $2.5 \text{ cm s}^{-1}$ . This offset can be better interpreted in terms of background shear when looking at the western, central, and eastern basin separately (Table 1). Background shear is analyzed as the velocity difference between 0.5 m and 15 m depth averaged between midnight and sunrise, that is, 0:00 to 6:00 LST. During this period, the DWL and hence the associated diurnal jet are removed by nocturnal mixing, and only the background shear remains. The seasonal and longitudinal variations of this background shear yield a range from  $1.2 \text{ cm s}^{-1}$  to  $11.8 \text{ cm s}^{-1}$  in the along-wind component with generally higher zonal background shear during the May experiment and higher meridional background shear during the October experiment. A comparison with the depth and strength of the EUC, which was generally shallower and stronger during the May compared to the October experiment (Brandt et al., 2023), indicates that zonal background shear is mainly related to the vertical migration and strength of the EUC core (Brandt et al., 2016).

The meridional background shear is strongest when enhanced meridional winds are present, that is, during the October drifter experiment and generally in the eastern basin. Marine radar and vmADCP measurements during the October ship transect reveal a strong positive correlation between the daily-mean meridional wind stress (ignoring the effect of the ocean surface velocity on  $\tau$ ) and the daily-mean vertical differences of meridional velocities, yielding a Pearson correlation coefficient of 0.81 using CCMP winds and 0.79 using ship's sensor winds. These correlations are significant at the 99%-level according to a Student's *t*-test. The correlations imply that, directly at the equator, a higher meridional wind stress results in higher meridional background shear. This is in line with the presence of the equatorial roll which is a shallow cross-equatorial overturning cell in the upper 80 m of the ocean with northward surface flow and a velocity reversal at about 25 m depth (Heukamp et al., 2022).

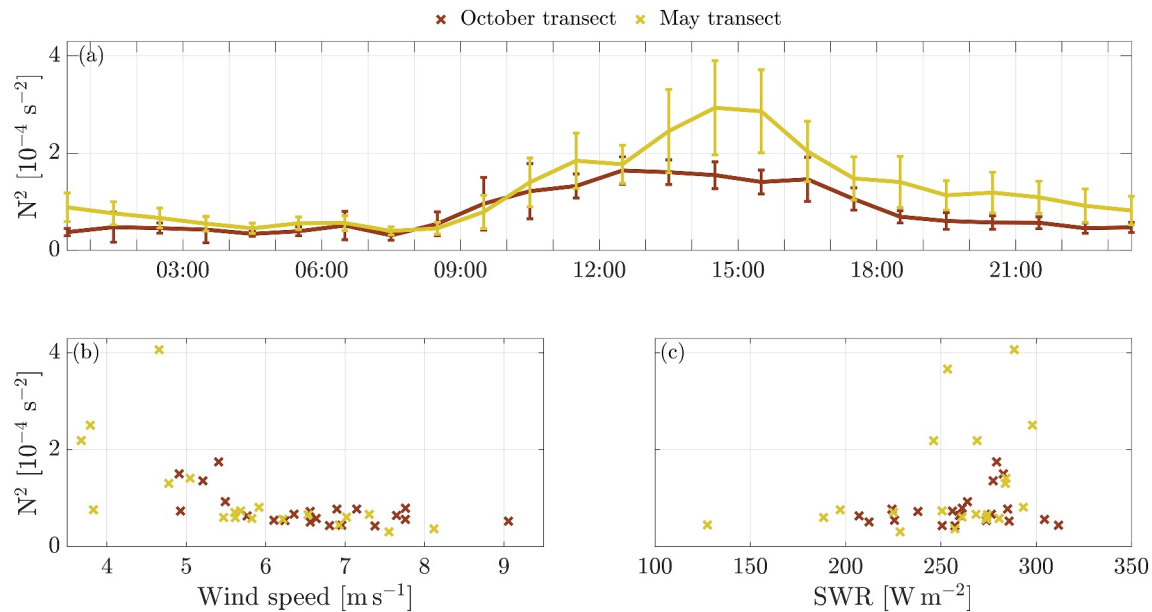


**Figure 4.** Stratification ( $N^2$ ) at 4 m depth as a function of LST, wind speed, and SWR. Mean diurnal cycles of  $N^2$  are shown (a) as a function of LST. The daily-mean  $N^2$  is shown as a function of (b) wind speed at 10 m height and (c) SWR. All parameters are derived from shipboard measurements during the May (yellow) and October (red) transects. The error bars in (a) represent the standard error.

The wind speed during both drifter experiments is comparable in the three basins, while the wind direction is turning about  $30^\circ$  westward from October to May and from the eastern to the western basin. Our results suggest that the seasonal and longitudinal differences in background conditions (wind direction and strength and depth of the EUC) mainly impact the background shear. The amplitude of the diurnal jet remains almost the same for both drifter experiments and across the basin (Table 1). With the wind speed being the only considered background condition that was similar for both drifter experiments, the wind speed might control the strength of the amplitude of the diurnal jet. This hypothesis about the wind speed influence will be tested in Section 5.

### 4.3. Observed Near-Surface Diurnal Stratification

Both ship transects are characterized by a diurnal cycle of near-surface stratification ( $N^2$ ) estimated at a depth of about 4 m which shows weak stratification at night and maximum stratification in the afternoon (Figure 4a), indicating the presence of a DWL. More precisely, the stratification is weakest about 1.5 hr after sunrise and reaches its maximum 0.5 hr (October transect) to 2.5 hr (May transect) after solar noon. While the diurnal cycles calculated for the two transects are aligned during the morning hours, there is higher near-surface stratification in the afternoon and at night for the May compared to the October transect.

The effect of wind speed and SWR on daily-mean  $N^2$  is shown in Figures 4b and 4c including the contribution of both the diurnal amplitude and night-time values. There are moderate to strong negative Spearman correlation coefficients between daily-mean wind speed and daily-mean stratification of  $-0.48$  for the October transect and  $-0.82$  for the May transect, which are significantly different from zero according to a permutation test, suggesting higher stratification for lower wind speeds and vice versa. Although the mean wind speeds only differed by  $1 \text{ m s}^{-1}$  between the two transects, days with low wind speeds ( $<4.5 \text{ m s}^{-1}$ ) occurred only during the May transect, resulting in a higher spread of daily-mean stratification values compared to the October transect (Figure 4b). This might also explain the higher mean diurnal  $N^2$  maximum for the May compared to the October transect. Furthermore, there appears to be a wind speed threshold of about  $5.5 \text{ m s}^{-1}$  that separates higher and lower spread of daily-mean stratification values at 4 m depth. A higher spread of stratification values can also be found for higher SWR (Figure 4c). As the occurrence of high daily-mean stratification coincides with both the presence of low wind speeds and high SWR, the wind speed threshold can be interpreted as a threshold below which SWR becomes important. This fits to earlier findings of the surface layer being more responsive to the heat

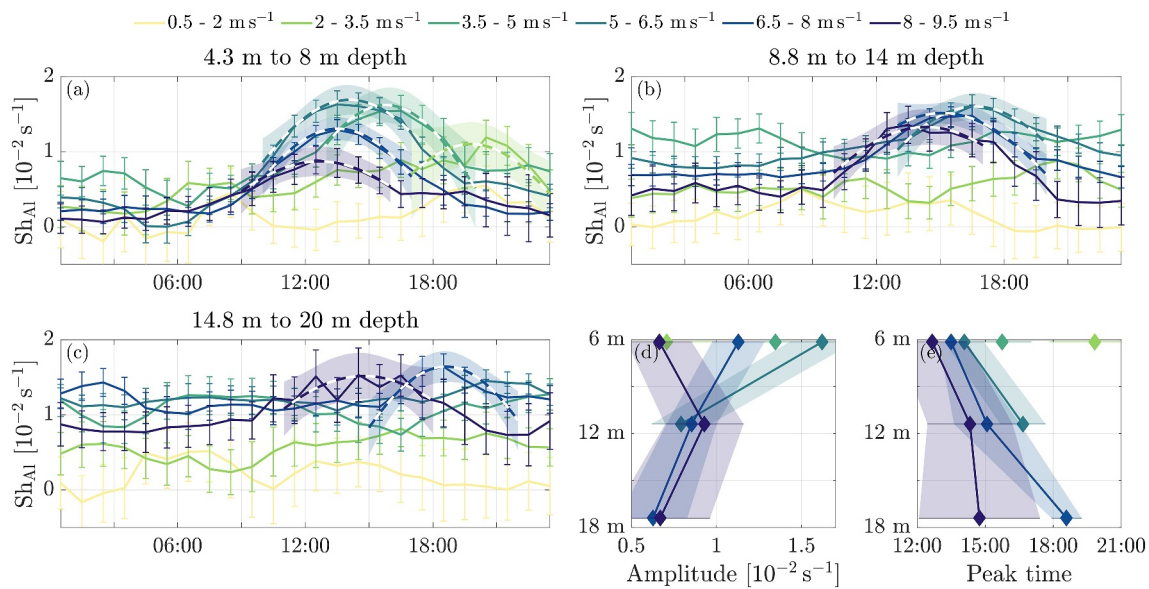


**Figure 5.** Mean diurnal cycles of along-wind shear ( $Sh_{AI}$ ) as a function of LST and wind speed.  $Sh_{AI}$  is derived between (a) 4.3 m and 8.0 m, (b) 8.8 m and 14.0 m, and (c) 14.8 m and 20.0 m depth for the PIRATA EMP at  $0^{\circ}N$ ,  $23^{\circ}W$ . If a robust diurnal pattern is present, the associated diurnal peak is fitted to a sinusoidal function which is displayed by the dashed line. For the three different depth ranges, (d) the diurnal amplitude of  $Sh_{AI}$  and (e) the timing of the diurnal peak are displayed. The colors correspond to different wind speed ranges. The vertical error bars represent the standard error, and the shading marks the 95% CIs to estimate the fitted peak.

flux at low wind speeds (Matthews et al., 2014). The effect of the wind speed on the diurnal stratification will be further analyzed in Section 5.

The observations indicate the presence of DWLs and associated diurnal jets during both measurement periods. While the diurnal cycles (amplitude and phase) of near-surface velocity differences were identical, the amplitude of diurnal near-surface stratification was larger for the May transect compared to the October transect. In this comparison it should be noted that the mean wind speed of the two drifter experiments, from which diurnal velocity cycles were derived, were similar while the mean wind speed of the two ship transects, from which the diurnal stratification cycles were derived, differed by  $1 \text{ m s}^{-1}$ . Hence, the wind speed might determine the amplitudes of not only the diurnal jet, as hypothesized earlier, but also of the DWL. In the following, the influence of the wind speed on the diurnal cycles of shear and stratification will be examined focusing on longer-term observations from the PIRATA buoy at  $0^{\circ}N$ ,  $23^{\circ}W$ .

## 5. Wind Speed Dependence of the Diurnal Cycles

In this section, we explore the dependence of near-surface shear and stratification on wind speed. For this purpose, mean diurnal cycles of  $Sh_{AI}$  and  $N^2$  are calculated where the respective values are binned into  $1.5 \text{ m s}^{-1}$  wind speed intervals.

To address the vertical structure and descent of the diurnal shear signal,  $Sh_{AI}$  is evaluated at 6.1 m depth (averaged between 4.3 m and 8.0 m, Figure 5a), 11.4 m depth (8.8 m and 14.0 m, Figure 5b), 17.4 m depth (14.8 m and 20.0 m, Figure 5c) as well as at 22.6 m depth (20.0 m and 25.3 m, not shown) derived from the PIRATA EMP at  $0^{\circ}N$ ,  $23^{\circ}W$ . For the deepest depth interval, no wind group shows robust diurnal characteristics as defined in Section 3.4. Wind speeds need to exceed  $2 \text{ m s}^{-1}$  for a robust diurnal jet to be detected at 6.1 m depth, exceed  $5 \text{ m s}^{-1}$  to be detected at 11.4 m depth, and exceed  $6.5 \text{ m s}^{-1}$  to be detected at 17.4 m depth. While at 6.1 m depth the diurnal amplitude of  $Sh_{AI}$  (Figure 5d) is largest for moderate winds, from 11.4 m depth downward, the diurnal amplitude increases with increasing wind speed. Considering the mean diurnal jet in the upper 15 m (Figure S3 in Supporting Information S1), both drifter experiments and the EMP agree to show an earlier diurnal peak with increasing wind speed while the diurnal amplitude is maximum for moderate wind speeds.

In general, the amplitude of  $Sh_{AI}$  decreases with increasing depth for every wind group, except for strongest winds of  $8 \text{ m s}^{-1}$  to  $9.5 \text{ m s}^{-1}$  where the amplitude just reaches its maximum at 11.4 m depth. The diurnal peak of  $Sh_{AI}$

**Table 2**  
Mean Descent Rates of the Peaks of  $N^2$  and  $Sh_{AI}$  as a Function of Wind Speed

Wind speed [ $m s^{-1}$ ]	2.0–3.5	3.5–5.0	5.0–6.5	6.5–8.0	8.0–9.5
Descent rate (Peak $N^2$ ) [ $m hr^{-1}$ ]	1.0	1.9	2.8	3.8	4.1
Descent rate (Peak $Sh_{AI}$ ) [ $m hr^{-1}$ ]	–	–	2.0	2.2	5.9

Note. The descent rates are calculated from the timings shown in Figures 5e and 6e for the PIRATA site at  $0^\circ N$ ,  $23^\circ W$ .

occurs later in the day with depth for all wind groups (Figure 5e). By fitting lines through the timing of the peaks at 6.1 m, 11.4 m and 17.4 m depth, we calculate mean descent rates of the shear maximum ranging from  $2.0 m hr^{-1}$  to  $5.9 m hr^{-1}$  (Table 2, Figure 7a).

To address the vertical structure and descent of the diurnal stratification signal,  $N^2$  is analyzed at 3 m depth (averaged between 1 m and 5 m, Figure 6a), 7.5 m depth (5 m and 10 m, Figure 6b), 15 m depth (10 m and 20 m, Figure 6c), and 30 m depth (20 m and 40 m, not shown) derived from the PIRATA buoy measurements at  $0^\circ N$ ,  $23^\circ W$ . At all these depths,  $N^2$  increases with decreasing wind speed, valid all day through. The standard error also increases with decreasing wind speed, indicating a higher spread in  $N^2$  values for weaker winds, in agreement with findings of the TRATLEQ transects (Section 4.3). At 3 m depth, the diurnal cycle of  $N^2$  is more pronounced at lower wind speeds, reaching amplitudes of  $6.7 \times 10^{-4} s^{-2}$  for the weakest and  $0.4 \times 10^{-4} s^{-2}$  for the strongest wind group (Figure 6d). This relation between the diurnal amplitude of  $N^2$  and the wind speed also applies to the other depths. However, the spread of the amplitudes reduces with depth. Wind speeds need to exceed  $2 m s^{-1}$  for a robust DWL to be detected at about 7.5 m depth and exceed  $3.5 m s^{-1}$  to be detected at about 15 m depth. There is no robust diurnal signal visible anymore at 30 m depth. Hence, the DWL reaches deeper for stronger winds but also becomes weaker. Note that our results give the impression that the DWL reaches deeper than the diurnal jet. We assume that this is solely a consequence of a reduced signal-to-noise ratio of the velocity data, leading to the signal of the descending diurnal jet being lost earlier than the one of the DWL. The maximum penetration depth for the DWL and the diurnal jet should be the same, as shown, for example, in Smyth et al. (2013).

The wind speed also affects the timing of the diurnal cycle of stratification with an earlier peak occurring for stronger winds (Figure 6e). The resulting spread of the peak times increases with depth. The descent of the maximum of  $N^2$  becomes faster with increasing wind speed with descent rates ranging between  $1.0 m hr^{-1}$  and

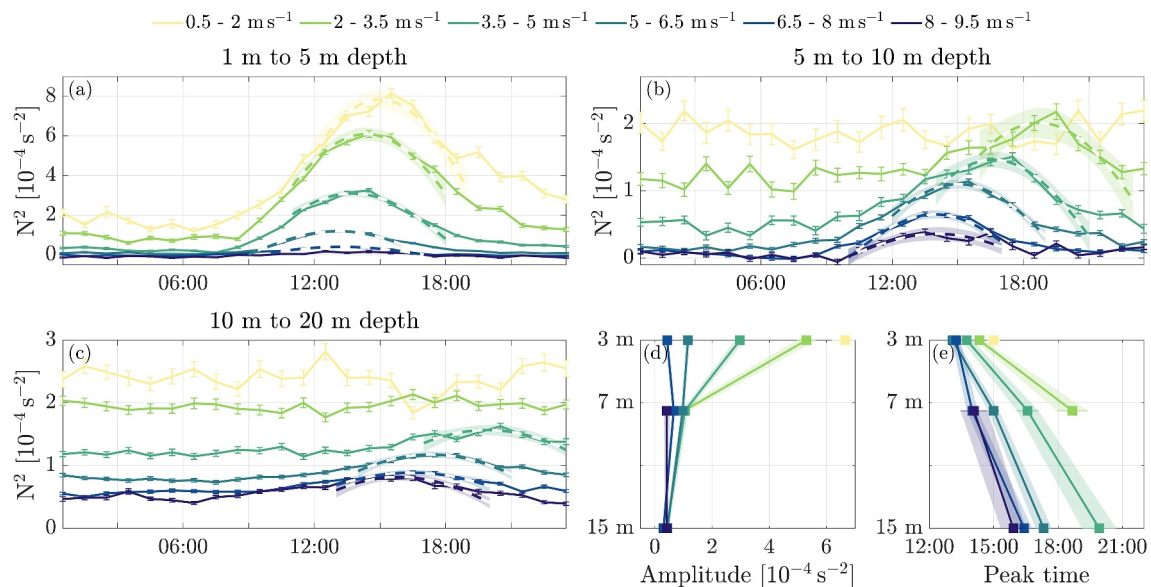


**Figure 6.** Mean diurnal cycles of stratification ( $N^2$ ) as a function of LST and wind speed.  $N^2$  is derived between (a) 1 m and 5 m, (b) 5 m and 10 m, and (c) 10 m and 20 m depth for the PIRATA site at  $0^\circ N$ ,  $23^\circ W$ . If a robust diurnal pattern is present, the associated diurnal peak is fitted to a sinusoidal function which is displayed by the dashed line. For the three different depth ranges, (d) the diurnal amplitude of  $N^2$  and (e) the timing of the diurnal peak are displayed. The colors correspond to different wind speed ranges. The vertical error bars represent the standard error, and the shading marks the 95% CIs to estimate the fitted peak.

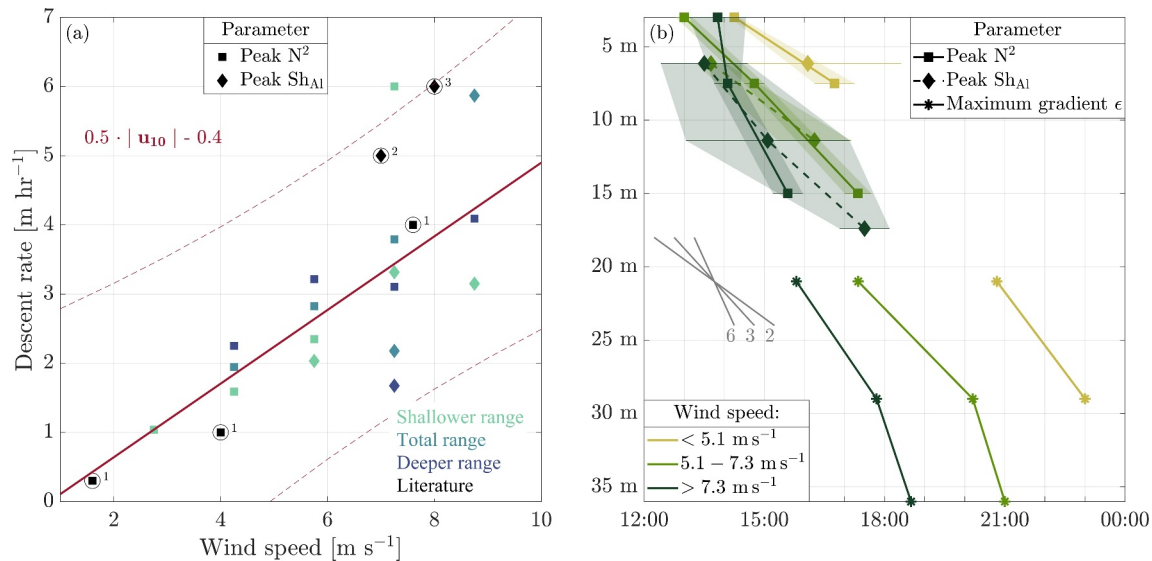


**Figure 7.** Descent of DWL, diurnal jet, and DCT. (a) Descent rates as a function of wind speed are calculated from the peaks of  $N^2$  (square) and  $Sh_{AI}$  (diamond) which are shown in Figures 5e and 6e for the shallower (light blue), deeper (dark blue) and total depth range (mid blue), derived from the PIRATA site at  $0^\circ N$ ,  $23^\circ W$ . The red lines represent a linear fit to the data (solid) and the associated 95% prediction interval (dashed). Literature descent rates (black and circled) are shown from (1) Hughes et al. (2020b), (2) Pham et al. (2017), and (3) Smyth et al. (2013). (b) Descent as a function of LST, depth, and wind speed at the PIRATA site at  $0^\circ N$ ,  $23^\circ W$ .  $N^2$  peaks (square),  $Sh_{AI}$  peaks (diamond), and the times of maximum temporal dissipation ( $\epsilon$ ) gradient (asterisk, from Figure 9 of Moum et al., 2023) are presented for three different wind groups in color. The shading marks the 95% CIs to estimate the fitted diurnal peak. As a reference for the descent rates, nominal slopes of  $2 \text{ m hr}^{-1}$ ,  $3 \text{ m hr}^{-1}$ , and  $6 \text{ m hr}^{-1}$  are indicated by the gray lines.

$4.1 \text{ m hr}^{-1}$  (Table 2, Figure 7a). According to the timing of the peaks, descent rates of both diurnal  $Sh_{AI}$  and  $N^2$  increase with increasing wind speed. Assuming a linear relationship between the wind speed and the descent rate yields that for every increase of  $2 \text{ m s}^{-1}$  in wind speed, the descent rate increases by  $1 \text{ m hr}^{-1}$  (Figure 7a). Note that this linear regression is computed excluding one  $Sh_{AI}$  peak as an outlier.

The timing and amplitude of the diurnal cycle of  $N^2$  at the PIRATA buoy at  $0^\circ N$ ,  $10^\circ W$  (Figure S4 in Supporting Information S1) are similar to those at  $0^\circ N$ ,  $23^\circ W$  presented before. The main differences between the mooring sites are a higher background stratification at 15 m depth and enhanced variability at 15 m depth obscuring the diurnal signal at  $10^\circ W$  compared to  $23^\circ W$ . The descent rates are also similar, yielding the same slope of the linear fit for the descent rate as a function of the wind speed at  $10^\circ W$  compared to  $23^\circ W$  (Figure S5a in Supporting Information S1).

## 6. Discussion

This study focuses on the diurnal cycles of shear and stratification, respectively associated with the diurnal jet and the DWL, in the upper 20 m of the equatorial Atlantic and on their wind dependence. Shear and stratification are primarily derived from drifter experiments and shipboard measurements during the TRATLEQ cruises in October 2019 and May 2022. The two periods differed in wind direction, net surface heat flux as well as strength and depth of the EUC but were comparable in wind speed. Despite these partly deviating conditions, similar timing and amplitude of diurnal jets and DWLs are observed.

The analyzed velocity and associated shear estimates correspond to different measurement methods which go along with different vertical ranges (drogue length of drifters, wave length of the dominant surface waves defining the depth range to which marine radar measurements refer, and bin size of the vmADCP), that are averaged to obtain the assigned depth values. Therefore, a comparison of the velocity and shear estimates is not straightforward and is subject to uncertainties. Additionally, the drifter measurements are affected by Stokes drift and wind slip (see Texts S2 and S1 in Supporting Information S1, respectively, for more details). Both, Stokes drift and wind slip, are assumed to have a negligible impact on the diurnal cycle. However, the mean Stokes drift of  $6 \text{ cm s}^{-1}$  can explain large parts of the background shear. The observed diurnal jet amplitudes are in the range of the previous observational results in the tropical and subtropical Atlantic and Pacific (Cronin & Kessler, 2009;

Kudryavtsev & Soloviev, 1990; Price et al., 1986; Sutherland et al., 2016; Wenegrat & McPhaden, 2015), although a direct comparison of diurnal jet diagnostics is complicated by the use of different depth levels and by different background and in particular wind conditions.

We observed a decrease in the diurnal amplitude of both the DWL and the associated diurnal jet with depth for all wind speeds (except for the diurnal jet at winds of  $8 \text{ m s}^{-1}$  to  $9.5 \text{ m s}^{-1}$ ). This suggests that the diurnal amplitudes will be underestimated if a shallowest useable depth of 11 m (Masich et al., 2021) or 10 m (Smyth et al., 2013) is used which stresses the importance of near-surface measurements to properly evaluate the near-surface heat and momentum budget.

### 6.1. Wind Speed Dependence of Diurnal Jet and Diurnal Warm Layer

The comparison of the two TRATLEQ periods suggests that the diurnal jet amplitude is independent, at least for conditions with mean wind speeds around  $6 \text{ m s}^{-1}$ , of the surface heat flux and the wind direction but might vary with wind speed. For conditions with low wind speeds, possibly the surface heat flux plays a role. The hypothesis of a wind speed dependence of the diurnal jet amplitude is tested and supported by examining observational records with a larger spread in wind conditions taken at the PIRATA buoys.

At the PIRATA buoy at  $0^\circ\text{N}$ ,  $23^\circ\text{W}$ , diurnal jets and DWLs are observed for wind speeds ranging from  $2 \text{ m s}^{-1}$  to  $9.5 \text{ m s}^{-1}$  and from  $0.5 \text{ m s}^{-1}$  to  $9.5 \text{ m s}^{-1}$ , respectively. Our results up to winds of  $9.5 \text{ m s}^{-1}$  do not support that there is a maximum wind speed threshold for the presence of both DWL and diurnal jet, as suggested by former studies (Kudryavtsev & Soloviev, 1990; Matthews et al., 2014; Thompson et al., 2019; Hughes et al., 2021). However, we do see a wind speed threshold of about  $5.5 \text{ m s}^{-1}$  above which the daily-mean stratification is clearly reduced. Accordingly, the discrepancy between our findings and previous studies might be a result of varying definitions of the DWL, especially with respect to thresholds such as minimum penetration depth and minimum diurnal amplitude.

The PIRATA measurements of both DWL and diurnal jet show a deeper descent and an earlier peak for stronger winds. For the DWL, the diurnal stratification amplitude increases with decreasing wind speed. For the diurnal jet, the diurnal shear amplitude at 6 m depth is maximum for moderate wind speeds of  $5 \text{ m s}^{-1}$  to  $6.5 \text{ m s}^{-1}$ . At 11 m depth and below, the diurnal shear amplitude is maximum for maximum wind speeds. Following the discussion on the dependence (Masich et al., 2021) or independence (Price et al., 1986; Sutherland et al., 2016) of the diurnal jet amplitude on wind speed, we would like to note that the above mentioned studies suggesting an independence are based on only a few days of measurements. Therefore, one possible explanation for the different conclusions on wind dependence might be the hypothesis of a memory of previous diurnal events (Sutherland et al., 2016). If a memory exists, changes in wind speed will have little influence on the diurnal diagnostics considering a time span of a few days but will be apparent in longer observational records. This could also explain the stronger variations in the diurnal jet amplitude as a function of wind speed for the PIRATA measurements compared to the drifter experiments.

### 6.2. Descent Rates of Diurnal Jet and Diurnal Warm Layer and Their Relation to Deep-Cycle Turbulence as a Function of Wind Speed

We find that the descent rates of shear and stratification peaks increase with wind speed. The respective descent rates are in line with observations for the descent of the stratification maximum observed by Hughes et al. (2020b) in the upper 2 m, 8 m, and 40 m in the subtropical Pacific for three different wind regimes. However, our descent rates are rather slower than the descent of shear maxima observed in the eastern equatorial Pacific by Pham et al. (2017) between 7.5 m and 17.5 m depth and by Smyth et al. (2013) between 15 m and 60 m depth (Figure 7a). The higher descent rates observed in the eastern equatorial Pacific compared to our findings in the equatorial Atlantic could indicate the presence of background conditions in the eastern equatorial Pacific that facilitate the descent. We expect that marginal instability could be such a condition as it was found to be more pronounced in the equatorial Pacific than in the equatorial Atlantic (Moum et al., 2023) and it is assumed to facilitate the descent of the diurnal jet (Lien et al., 1995; Masich et al., 2021). However, marginal instability has not been analyzed in this study and further research is needed to identify the causalities of possible different descent rates in the equatorial Atlantic and Pacific.

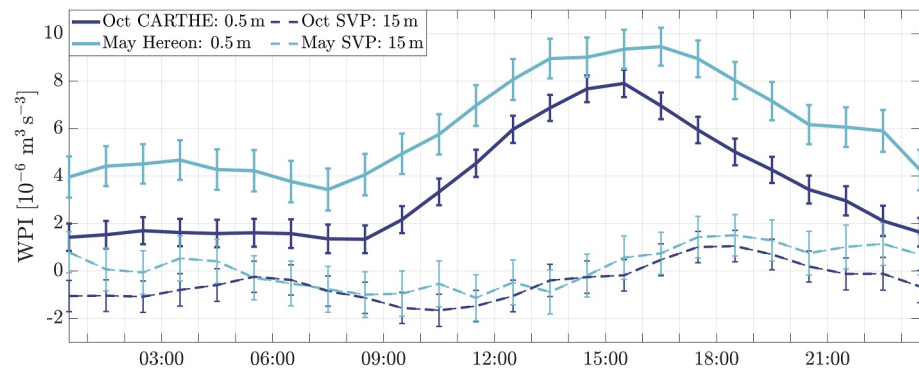


**Figure 8.** Mean diurnal cycles of wind power input (WPI) as a function of LST. The WPI is computed for the May (light blue) and October (dark blue) drifter experiments by using velocities at 0.5 m (solid lines) and at 15 m (dashed lines) depth. The error bars represent the standard error.

The observed timing of the diurnal stratification and shear peaks as a function of depth and wind speed can be used to examine the hypothesis of Moum et al. (2023) that the wind-dependent delay of DCT may be a direct result of the wind-dependent DWL deepening. Both the maximum temporal dissipation gradient found by Moum et al. (2023) and the peak of stratification and shear at the PIRATA mooring sites (Figure 7b) show an earlier onset or peak, respectively, for stronger winds. This is also true at the PIRATA site at 0°N, 10°W (Figure S5b in Supporting Information S1) and indicates that the wind-dependent descent rates of the DWL and the diurnal jet indicated in this study also reflect in the timing of DCT. However, it remains unclear when and where instabilities are triggered. The exact timing of the onset and the peak of diurnal shear, shear instabilities and DCT might also depend on background stratification and shear. We suggest that studying DCT as a function of wind speed can help to relate the wind-dependent descending diurnal jet to DCT, for which Moum et al. (2023) found a wind dependence of the strength but not of the descent rate. Note that also the wind-dependent strength of DCT might be explained by the wind-dependent penetration depth and amplitude of the diurnal jet.

### 6.3. Impact of the Diurnal Cycle on the Wind Power Input

The near-surface diurnal dynamics described in this study also reflect in the WPI (Figure 8) and thus impact the amount of mechanical energy transferred from the atmosphere into the ocean. The WPI is calculated as the scalar product of the wind stress and the ocean surface velocity (see Section 3.5). Therefore, both the changes in the ocean velocity during the day and the angle between the wind and the ocean current matter for the magnitude of the WPI. The WPI derived from the drifter velocities at 0.5 m depth is characterized by a diurnal cycle. This diurnal cycle leads to a  $1.62 \times 10^{-6} \text{ m}^3 \text{ s}^{-3}$ , that is, 59%, and a  $1.60 \times 10^{-6} \text{ m}^3 \text{ s}^{-3}$ , that is, 32%, increase of the diurnal mean WPI compared to the night-time WPI for the October and the May drifter experiment, respectively. The diurnal cycles also resemble a simulated diurnal magnitude of wind work at 10°N regarding the timing of the onset and the peak (Schmitt et al., 2024). The calculation of a supposed WPI using the October and May drifter velocities at 15 m depth leads to a reduction of the WPI by 80% and 96%, respectively. This underestimation of the available surface kinetic energy stresses the relevance of considering the diurnal jet and of actually observing surface velocities instead of taking, for example, 15 m velocities as surface velocities. Furthermore, it shows that DWL and diurnal jet not only impact energy transfer into the mixed layer but also impact air-sea fluxes and the amount of energy within the DWL and below which is available for mixing.

## 7. Conclusion

This study examines the diurnal warm layer and associated diurnal jet in the equatorial Atlantic, focusing on the influence of wind speed on their characteristics. Our analysis demonstrates that wind speed influences timing, amplitude, penetration depth, and descent rate of diurnal warm layer and associated diurnal jet. The wind-dependent descent rate of the diurnal jet and the diurnal warm layer can explain the wind-dependent onset of deep-cycle turbulence. Furthermore, the diurnal dynamics impact the energy input into the ocean through modulation of the wind power input. The question of how much of this energy is used to enhance turbulence during the descent of the diurnal warm layer in the deep-cycle turbulence layer remains open.

Our results enhance the understanding of diurnal dynamics and stress the importance of near-surface measurements of, in particular, velocity. We want to emphasize that future satellite missions aiming to resolve absolute ocean currents could provide additional data for better regional characterization of diurnal surface velocity variability (Ardhuin et al., 2019; Villas Bôas et al., 2019). Our results and in particular the TRATLEQ velocity data sets, which allow for a basin-scale view of velocities and shear in the upper meters of the ocean, can contribute to calibrate and validate satellite missions that aim to infer absolute surface currents like the current SWOT mission (Morrow et al., 2019) or possible future missions based on advanced Doppler-radar techniques as suggested for ODYSEA (Rodríguez et al., 2019) or SKIM (Ardhuin et al., 2018). Our results will enable the examination of possible offsets of satellite measurements due to sampling at various hours of the day. This study can also facilitate the validation of ocean models that resolve diurnal dynamics (Bernie et al., 2007), aim to be energetically consistent (Eden et al., 2014; Gutjahr et al., 2021), or aim to correctly represent surface currents for other applications, for example, to deduce Sargassum drift (Van Sebille et al., 2021). Moreover, this study points out that the diurnal cycle can be captured by vessel-mounted observation systems, which might be useful for further studies on spatial pattern of diurnal dynamics.

### Data Availability Statement

The marine radar and vmADCP measurements used to derive 3 m and 17 m depth en-route ocean velocities during the October transect are available at Pangaea in Carrasco et al. (2024) and in Brandt et al. (2022), respectively. The drifter data used to derive velocities at 0.5 m and 15 m depth for the October drifter experiment are available at Pangaea in Hans and Brandt (2021) with the ID/WMO numbers of the used SVP drifters listed in Table S1 of Supporting Information S1. For the May drifter experiment, the Hereon drifter positions are available at Pangaea in Horstmann et al. (2023) and the SVP drifter positions at NOAA's OSMC ERDDAP via <https://www.aoml.noaa.gov/phod/gdp/data.php> with the relevant ID/WMO numbers listed in Table S2 of Supporting Information S1. TSG, pitch, and roll data used to derive a stratification estimate at 4 m depth as well as wind and radiation data for the two TRATLEQ cruises are available at the Dship system via [dship.bsh.de](https://dship.bsh.de). Temperature, salinity, and wind data from the PIRATA buoys used in this study are available from the Global Tropical Moored Buoy Array at <https://www.pmel.noaa.gov/tao/drupal/disdel/>. The access to the heat flux data used from ePIRATA is described at <https://www.aoml.noaa.gov/phod/epirata/>. The velocity data at the PIRATA site at 0°N, 23°W during the EMP are available at [https://www.pmel.noaa.gov/tao/drupal/disdel/adcp\\_0n23w/index.html](https://www.pmel.noaa.gov/tao/drupal/disdel/adcp_0n23w/index.html). The satellite CCMP V2.0 wind data are available at REMSS via [www.remss.com](http://www.remss.com) (Wentz et al., 2015). All analyses were performed and all figures created using MATLAB R2021a.

### References

- Ardhuin, F., Aksenov, Y., Benetazzo, A., Bertino, L., Brandt, P., Caubet, E., et al. (2018). Measuring currents, ice drift, and waves from space: The sea surface Kinematics multiscale monitoring (SKIM) concept. *Ocean Science*, 14(3), 337–354. <https://doi.org/10.5194/os-14-337-2018>
- Ardhuin, F., Brandt, P., Gaultier, L., Donlon, C., Battaglia, A., Boy, F., et al. (2019). SKIM, a candidate satellite mission exploring global ocean currents and waves. *Frontiers in Marine Science*, 6, 209. <https://doi.org/10.3389/fmars.2019.00209>
- Atlas, R., Hoffman, R. N., Ardizzone, J., Leidner, S. M., Jusem, J. C., Smith, D. K., & Gombos, D. (2011). A cross-calibrated, multiplatform ocean surface wind velocity product for meteorological and oceanographic applications. *Bulletin of the American Meteorological Society*, 92(2), 157–174. <https://doi.org/10.1175/2010BAMS2946.1>
- Bellenger, H., & Duvel, J.-P. (2009). An analysis of tropical ocean diurnal warm layers. *Journal of Climate*, 22(13), 3629–3646. <https://doi.org/10.1175/2008JCL12598.1>
- Bernie, D. J., Guilyardi, E., Madec, G., Slingo, J. M., & Woolnough, S. J. (2007). Impact of resolving the diurnal cycle in an ocean–atmosphere GCM. Part 1: A diurnally forced OGCM. *Climate Dynamics*, 29(6), 575–590. <https://doi.org/10.1007/s00382-007-0249-6>
- Bouřlès, B., Araujo, M., McPhaden, M. J., Brandt, P., Foltz, G. R., Lumpkin, R., et al. (2019). Pirata: A sustained observing system for tropical Atlantic climate research and forecasting. *Earth and Space Science*, 6(4), 577–616. <https://doi.org/10.1029/2018EA000428>
- Brandt, P., Alory, G., Awo, F. M., Dengler, M., Djakouré, S., Imbol Koungue, R. A., et al. (2023). Physical processes and biological productivity in the upwelling regions of the tropical Atlantic. *Ocean Science*, 19(3), 581–601. <https://doi.org/10.5194/os-19-581-2023>
- Brandt, P., Claus, M., Greatbatch, R. J., Kopte, R., Toole, J. M., Johns, W. E., & Böning, C. W. (2016). Annual and semiannual cycle of equatorial Atlantic circulation associated with basin-mode resonance. *Journal of Physical Oceanography*, 46(10), 3011–3029. <https://doi.org/10.1175/JPO-D-15-0248.1>
- Brandt, P., Czeschel, R., & Krahnmann, G. (2022). ADCP current measurements (38 and 75 kHz) during METEOR cruise M158 [Dataset]. <https://doi.org/10.1594/PANGAEA.952101>
- Carrasco, R., Horstmann, J., & Brandt, P. (2024). Radar-derived surface current fields along RV METEOR cruise track M158 [Dataset]. <https://doi.org/10.1594/PANGAEA.965702>
- Cronin, M. F., & Kessler, W. S. (2009). Near-surface shear flow in the tropical Pacific cold tongue front. *Journal of Physical Oceanography*, 39(5), 1200–1215. <https://doi.org/10.1175/2008JPO4064.1>
- Delnoro, V. E. (1972). Diurnal variation of temperature and energy budget for the oceanic mixed layer during BOMEX. *Journal of Physical Oceanography*, 2(3), 239–247. [https://doi.org/10.1175/1520-0485\(1972\)002<0239:DVOTAE>2.0.CO;2](https://doi.org/10.1175/1520-0485(1972)002<0239:DVOTAE>2.0.CO;2)



- Donlon, C. J., Minnett, P. J., Gentemann, C., Nightingale, T. J., Barton, I. J., Ward, B., & Murray, M. J. (2002). Toward improved validation of satellite sea surface skin temperature measurements for climate research. *Journal of Climate*, *15*(4), 353–369. [https://doi.org/10.1175/1520-0442\(2002\)015<0353:TIVOSS>2.0.CO;2](https://doi.org/10.1175/1520-0442(2002)015<0353:TIVOSS>2.0.CO;2)
- Dutton, J. A. (1995). *Dynamics of atmospheric motion (Unabridged and unaltered reproduction)*. Dover Publications.
- Eden, C., Czeschel, L., & Olbers, D. (2014). Toward energetically consistent ocean models. *Journal of Physical Oceanography*, *44*(12), 3160–3184. <https://doi.org/10.1175/JPO-D-13-0260.1>
- Efron, B. (1979). Bootstrap methods: Another look at the Jackknife. *Annals of Statistics*, *7*(1). <https://doi.org/10.1214/aos/1176344552>
- Elipot, S., & Wenegrat, J. O. (2021). Vertical Structure of near-surface currents - importance, state of knowledge, and measurement challenges. *US Clivar Variations*, *19*(1). <https://doi.org/10.5065/YBCA-0S03>
- Fischer, J., Brandt, P., Dengler, M., Müller, M., & Symonds, D. (2003). Surveying the upper ocean with the ocean Surveyor: A new phased Array Doppler current profiler. *Journal of Atmospheric and Oceanic Technology*, *20*(5), 742–751. [https://doi.org/10.1175/1520-0426\(2003\)20<742:STUOWT>2.0.CO;2](https://doi.org/10.1175/1520-0426(2003)20<742:STUOWT>2.0.CO;2)
- Fischer, T., Kock, A., Arévalo-Martínez, D. L., Dengler, M., Brandt, P., & Bange, H. W. (2019). Gas exchange estimates in the Peruvian upwelling regime biased by multi-day near-surface stratification. *Biogeosciences*, *16*(11), 2307–2328. <https://doi.org/10.5194/bg-16-2307-2019>
- Fleagle, R. G., & Businger, J. A. (1980). *An introduction to atmospheric physics* (2d ed). Academic Press.
- Foltz, G. R., Schmid, C., & Lumpkin, R. (2018). An enhanced PIRATA dataset for tropical Atlantic Ocean–atmosphere research. *Journal of Climate*, *31*(4), 1499–1524. <https://doi.org/10.1175/JCLI-D-16-0816.1>
- Gentemann, C. L., & Minnett, P. J. (2008). Radiometric measurements of ocean surface thermal variability. *Journal of Geophysical Research*, *113*(C8), 2007JC004540. <https://doi.org/10.1029/2007JC004540>
- Gentemann, C. L., Minnett, P. J., & Ward, B. (2009). Profiles of ocean surface heating (POSH): A new model of upper ocean diurnal warming. *Journal of Geophysical Research*, *114*(C7), C07017. <https://doi.org/10.1029/2008JC004825>
- Gutjahr, O., Brüggemann, N., Haak, H., Jungclauss, J. H., Putrasahan, D. A., Lohmann, K., & Von Storch, J.-S. (2021). Comparison of ocean vertical mixing schemes in the max planck Institute Earth system model (MPI-ESM1.2). *Geoscientific Model Development*, *14*(5), 2317–2349. <https://doi.org/10.5194/gmd-14-2317-2021>
- Hans, A. C., & Brandt, P. (2021). Surface drifter data from Meteor cruise M158 [Dataset]. <https://doi.org/10.1594/PANGAEA.926752>
- Heukamp, F. O., Brandt, P., Dengler, M., Tuchen, F. P., McPhaden, M. J., & Moum, J. N. (2022). Tropical instability waves and wind-forced cross-equatorial flow in the central Atlantic Ocean. *Geophysical Research Letters*, *49*(19), e2022GL099325. <https://doi.org/10.1029/2022GL099325>
- Horstmann, J., Bödewadt, J., Carrasco, R., Cysewski, M., Seemann, J., & Streßer, M. (2021). A coherent on receive X-band marine Radar for ocean observations. *Sensors*, *21*(23), 7828. <https://doi.org/10.3390/s21237828>
- Horstmann, J., Borge, J. C. N., Seemann, J., Carrasco, R., & Lund, B. (2015). Wind, wave, and current retrieval utilizing X-band marine radars. In *Coastal Ocean observing systems* (pp. 281–304). Elsevier. <https://doi.org/10.1016/B978-0-12-802022-7.00016-X>
- Horstmann, J., Navarro, W., Carrasco, R., Brandt, P., Hans, A. C., & Prigent, A. (2023). Surface drifter data of the equatorial Atlantic: Positions of Lagrangian Hereon drifters deployed in the equatorial Atlantic during METEOR cruise M181 [Dataset]. <https://doi.org/10.1594/PANGAEA.955925>
- Hughes, K. G., Moum, J. N., & Shroyer, E. L. (2020a). Evolution of the velocity structure in the diurnal warm layer. *Journal of Physical Oceanography*, *50*(3), 615–631. <https://doi.org/10.1175/JPO-D-19-0207.1>
- Hughes, K. G., Moum, J. N., & Shroyer, E. L. (2020b). Heat Transport through diurnal warm layers. *Journal of Physical Oceanography*, *50*(10), 2885–2905. <https://doi.org/10.1175/JPO-D-20-0079.1>
- Hughes, K. G., Moum, J. N., Shroyer, E. L., & Smyth, W. D. (2021). Stratified shear instabilities in diurnal warm layers. *Journal of Physical Oceanography*. <https://doi.org/10.1175/JPO-D-20-0300.1>
- IOC / SCOR / IAPSO. (2010). The international thermodynamic equation of seawater - 2010: Calculation and use of thermodynamic properties. *Intergovernmental Oceanographic Commission, Manuals and Guides*, 56. Retrieved from [https://www.teos-10.org/pubs/TEOS-10\\_Manual.pdf](https://www.teos-10.org/pubs/TEOS-10_Manual.pdf)
- Kawai, Y., Kawamura, H., Tanba, S., Ando, K., Yoneyama, K., & Nagahama, N. (2006). Validity of sea surface temperature observed with the TRITON buoy under diurnal heating conditions. *Journal of Oceanography*, *62*(6), 825–838. <https://doi.org/10.1007/s10872-006-0101-3>
- Kawai, Y., & Wada, A. (2007). Diurnal sea surface temperature variation and its impact on the atmosphere and ocean: A review. *Journal of Oceanography*, *63*(5), 721–744. <https://doi.org/10.1007/s10872-007-0063-0>
- Koblick, D. (2021). Convert UTC to solar apparent time. Retrieved from <https://www.mathworks.com/matlabcentral/fileexchange/32804-convert-utc-to-solar-apparent-time>
- Kudryavtsev, V. N., & Soloviev, A. V. (1990). Slippery near-surface layer of the ocean arising due to daytime solar heating. *Journal of Physical Oceanography*, *20*(5), 617–628. [https://doi.org/10.1175/1520-0485\(1990\)020<0617:SNSLOT>2.0.CO;2](https://doi.org/10.1175/1520-0485(1990)020<0617:SNSLOT>2.0.CO;2)
- Laurent, L., St., & Merrifield, S. (2017). Measurements of near-surface turbulence and mixing from autonomous ocean gliders. *Oceanography*, *30*(2), 116–125. <https://doi.org/10.5670/oceanog.2017.231>
- Lien, R.-C., Caldwell, D. R., Gregg, M. C., & Moum, J. N. (1995). Turbulence variability at the equator in the central Pacific at the beginning of the 1991–1993 El Niño. *Journal of Geophysical Research*, *100*(C4), 6881–6898. <https://doi.org/10.1029/94JC03312>
- Lund, B., Haus, B. K., Horstmann, J., Graber, H. C., Carrasco, R., Laxague, N. J. M., et al. (2018). Near-surface current mapping by shipboard marine X-band radar: A validation. *Journal of Atmospheric and Oceanic Technology*, *35*(5), 1077–1090. <https://doi.org/10.1175/JTECH-D-17-0154.1>
- Masich, J., Kessler, W. S., Cronin, M. F., & Grissom, K. R. (2021). Diurnal cycles of near-surface currents across the tropical Pacific. *Journal of Geophysical Research: Oceans*, *126*(4), e2020JC016982. <https://doi.org/10.1029/2020JC016982>
- Matthews, A. J., Baranowski, D. B., Heywood, K. J., Flatau, P. J., & Schmidt, S. (2014). The surface diurnal warm layer in the Indian ocean during CINDY/DYNAMO. *Journal of Climate*, *27*(24), 9101–9122. <https://doi.org/10.1175/JCLI-D-14-00222.1>
- Morrow, R., Fu, L.-L., Arduin, F., Benkiran, M., Chapron, B., Cosme, E., et al. (2019). Global observations of fine-scale ocean surface topography with the surface water and ocean topography (SWOT) mission. *Frontiers in Marine Science*, *6*, 232. <https://doi.org/10.3389/fmars.2019.00232>
- Moum, J. N., & Caldwell, D. R. (1985). Local influences on shear-flow turbulence in the equatorial ocean. *Science*, *230*(4723), 315–316. <https://doi.org/10.1126/science.230.4723.315>
- Moum, J. N., Hughes, K. G., Shroyer, E. L., Smyth, W. D., Cherian, D., Warner, S. J., et al. (2022). Deep cycle turbulence in Atlantic and Pacific cold tongues. *Geophysical Research Letters*, *49*(8), e2021GL097345. <https://doi.org/10.1029/2021GL097345>
- Moum, J. N., Perlin, A., Nash, J. D., & McPhaden, M. J. (2013). Seasonal sea surface cooling in the equatorial Pacific cold tongue controlled by ocean mixing. *Nature*, *500*(7460), 64–67. <https://doi.org/10.1038/nature12363>

- Moum, J. N., Smyth, W. D., Hughes, K. G., Cherian, D., Warner, S. J., Bourlès, B., et al. (2023). Wind dependencies of deep cycle turbulence in the equatorial cold tongues. *Journal of Physical Oceanography*, 53(8), 1979–1995. <https://doi.org/10.1175/JPO-D-22-0203.1>
- Pacanowski, R. C. (1987). Effect of equatorial currents on surface stress. *Journal of Physical Oceanography*, 17(6), 833–838. [https://doi.org/10.1175/1520-0485\(1987\)017<0833:EOECOS>2.0.CO;2](https://doi.org/10.1175/1520-0485(1987)017<0833:EOECOS>2.0.CO;2)
- Peters, H., Gregg, M. C., & Toole, J. M. (1988). On the parameterization of equatorial turbulence. *Journal of Geophysical Research*, 93(C2), 1199–1218. <https://doi.org/10.1029/JC093iC02p01199>
- Pham, H. T., Sarkar, S., & Winters, K. B. (2013). Large-eddy simulation of deep-cycle turbulence in an equatorial undercurrent model. *Journal of Physical Oceanography*, 43(11), 2490–2502. <https://doi.org/10.1175/JPO-D-13-016.1>
- Pham, H. T., Smyth, W. D., Sarkar, S., & Moum, J. N. (2017). Seasonality of deep cycle turbulence in the eastern equatorial Pacific. *Journal of Physical Oceanography*, 47(9), 2189–2209. <https://doi.org/10.1175/JPO-D-17-0008.1>
- Price, J. F., Weller, R. A., & Pinkel, R. (1986). Diurnal cycling: Observations and models of the upper ocean response to diurnal heating, cooling, and wind mixing. *Journal of Geophysical Research*, 91(C7), 8411–8427. <https://doi.org/10.1029/JC091iC07p08411>
- Radenac, M.-H., Jouanno, J., Tchamabi, C. C., Awo, M., Bourlès, B., Arnault, S., & Aumont, O. (2020). Physical drivers of the nitrate seasonal variability in the Atlantic cold tongue. *Biogeosciences*, 17(2), 529–545. <https://doi.org/10.5194/bg-17-529-2020>
- Rodríguez, E., Bourassa, M., Chelton, D., Farrar, J. T., Long, D., Perkovic-Martin, D., & Samelson, R. (2019). The winds and currents mission concept. *Frontiers in Marine Science*, 6, 438. <https://doi.org/10.3389/fmars.2019.00438>
- Röhrs, J., Sutherland, G., Jeans, G., Bedington, M., Sperreik, A. K., Dagestad, K.-F., et al. (2021). Surface currents in operational oceanography: Key applications, mechanisms, and methods. *Journal of Operational Oceanography*, 16(1), 60–88. <https://doi.org/10.1080/1755876X.2021.1903221>
- Schmitt, M., Pham, H. T., Sarkar, S., Klingbeil, K., & Umlauf, L. (2024). Diurnal Warm Layers in the ocean: Energetics, non-dimensional scaling, and parameterization. *Journal of Physical Oceanography*, 54(4), 1037–1055. <https://doi.org/10.1175/JPO-D-23-0129.1>
- Smyth, W. D., & Moum, J. N. (2013). Marginal instability and deep cycle turbulence in the eastern equatorial Pacific Ocean. *Geophysical Research Letters*, 40(23), 6181–6185. <https://doi.org/10.1002/2013GL058403>
- Smyth, W. D., Moum, J. N., Li, L., & Thorpe, S. A. (2013). Diurnal shear instability, the descent of the surface shear layer, and the deep cycle of equatorial turbulence. *Journal of Physical Oceanography*, 43(11), 2432–2455. <https://doi.org/10.1175/JPO-D-13-089.1>
- Smyth, W. D., Nash, J. D., & Moum, J. N. (2019). Self-organized criticality in geophysical turbulence. *Scientific Reports*, 9(1), 3747. <https://doi.org/10.1038/s41598-019-39869-w>
- Soloviev, A., & Lukas, R. (1997). Observation of large diurnal warming events in the near-surface layer of the western equatorial Pacific warm pool. *Deep Sea Research Part I: Oceanographic Research Papers*, 44(6), 1055–1076. [https://doi.org/10.1016/S0967-0637\(96\)00124-0](https://doi.org/10.1016/S0967-0637(96)00124-0)
- Soloviev, A., & Lukas, R. (2014). *The near-surface layer of the ocean: Structure, dynamics and applications* (Vol. 48). Springer Netherlands. <https://doi.org/10.1007/978-94-007-7621-0>
- Sutherland, G., Marié, L., Reverdin, G., Christensen, K. H., Broström, G., & Ward, B. (2016). Enhanced turbulence associated with the diurnal jet in the ocean surface boundary layer. *Journal of Physical Oceanography*, 46(10), 3051–3067. <https://doi.org/10.1175/JPO-D-15-0172.1>
- Thompson, E. J., Moum, J. N., Fairall, C. W., & Rutledge, S. A. (2019). Wind limits on rain layers and diurnal warm layers. *Journal of Geophysical Research: Oceans*, 124(2), 897–924. <https://doi.org/10.1029/2018JC014130>
- Van Sebille, E., Zettler, E., Wienders, N., Amaral-Zettler, L., Elipot, S., & Lumpkin, R. (2021). Dispersion of surface drifters in the tropical Atlantic. *Frontiers in Marine Science*, 7, 607426. <https://doi.org/10.3389/fmars.2020.607426>
- Villas Bôas, A. B., Ardhuin, F., Ayet, A., Bourassa, M. A., Brandt, P., Chapron, B., et al. (2019). Integrated observations of global surface winds, currents, and waves: Requirements and challenges for the next decade. *Frontiers in Marine Science*, 6, 425. <https://doi.org/10.3389/fmars.2019.00425>
- Waliser, D. E., & Gautier, C. (1993). A satellite-derived climatology of the ITCZ. *Journal of Climate*, 6(11), 2162–2174. [https://doi.org/10.1175/1520-0442\(1993\)006<2162:ASDCOT>2.0.CO;2](https://doi.org/10.1175/1520-0442(1993)006<2162:ASDCOT>2.0.CO;2)
- Ward, B. (2006). Near-surface ocean temperature. *Journal of Geophysical Research*, 111(C2), 2004JC002689. <https://doi.org/10.1029/2004JC002689>
- Wenegrat, J. O., & McPhaden, M. J. (2015). Dynamics of the surface layer diurnal cycle in the equatorial Atlantic Ocean (0°, 23°W). *Journal of Geophysical Research: Oceans*, 120(1), 563–581. <https://doi.org/10.1002/2014JC010504>
- Wenegrat, J. O., McPhaden, M. J., & Lien, R. (2014). Wind stress and near-surface shear in the equatorial Atlantic Ocean. *Geophysical Research Letters*, 41(4), 1226–1231. <https://doi.org/10.1002/2013GL059149>
- Wentz, F. J., Scott, J., Hoffmann, R., Leidner, M., & Atlas, R. (2015). Remote Sensing Systems Cross-Calibrated Multi-Platform (CCMP) 6-hourly ocean vector wind analysis product on 0.25 deg grid, Version 2.0 [Dataset]. Remote Sensing Systems. Retrieved from <https://www.remss.com/measurements/ccmp/>
- Whitt, D. B., Cherian, D. A., Holmes, R. M., Bachman, S. D., Lien, R.-C., Large, W. G., & Moum, J. N. (2022). Simulation and scaling of the turbulent vertical heat transport and deep-cycle turbulence across the equatorial Pacific cold tongue. *Journal of Physical Oceanography*, 52(5), 981–1014. <https://doi.org/10.1175/JPO-D-21-0153.1>
- Woods, J. D., & Strass, V. (1986). The response of the upper ocean to solar heating II: The wind-driven current. *Quarterly Journal of the Royal Meteorological Society*, 112(471), 29–42. <https://doi.org/10.1002/qj.49711247103>

## References From the Supporting Information

- C3S. (2018). ERA5 hourly data on single levels from 1940 to present [Dataset]. <https://doi.org/10.24381/CDS.ADBB2D47>
- Carrasco, A., Semedo, A., Isachsen, P. E., Christensen, K. H., & Saetra, Ø. (2014). Global surface wave drift climate from ERA-40: The contributions from wind-sea and swell. *Ocean Dynamics*, 64(12), 1815–1829. <https://doi.org/10.1007/s10236-014-0783-9>
- CMEMS. (2019). Global Ocean waves reanalysis WAWERYYS [Dataset]. <https://doi.org/10.48670/MOI-00022>
- Haza, A. C., D'Asaro, E., Chang, H., Chen, S., Curcic, M., Guigand, C., et al. (2018). Drogue-loss detection for surface drifters during the Lagrangian submesoscale experiment (LASER). *Journal of Atmospheric and Oceanic Technology*, 35(4), 705–725. <https://doi.org/10.1175/JTECH-D-17-0143.1>
- Kenyon, K. E. (1969). Stokes drift for random gravity waves. *Journal of Geophysical Research*, 74(28), 6991–6994. <https://doi.org/10.1029/JC074i028p06991>
- Lodise, J., Özgökmen, T., Griffa, A., & Berta, M. (2019). Vertical structure of ocean surface currents under high winds from massive arrays of drifters. *Ocean Science*, 15(6), 1627–1651. <https://doi.org/10.5194/os-15-1627-2019>

- Lumpkin, R., & Pazos, M. (2007). Measuring surface currents with surface velocity Program drifters: The instrument, its data, and some recent results. In A. Griffa, A. D. Kirwan, Jr., A. J. Mariano, T. Özgökmen, & H. T. Rossby (Eds.), *Lagrangian analysis and prediction of coastal and ocean dynamics* (1st ed., pp. 39–67). Cambridge University Press. <https://doi.org/10.1017/CBO9780511535901.003>
- Niiler, P. P., Sybrandt, A. S., Bi, K., Poulain, P. M., & Bitterman, D. (1995). Measurements of the water-following capability of holey-sock and TRISTAR drifters. *Deep Sea Research Part I: Oceanographic Research Papers*, 42(11–12), 1951–1964. [https://doi.org/10.1016/0967-0637\(95\)00076-3](https://doi.org/10.1016/0967-0637(95)00076-3)
- Novelli, G., Guigand, C. M., Cousin, C., Ryan, E. H., Laxague, N. J. M., Dai, H., et al. (2017). A biodegradable surface drifter for ocean sampling on a massive scale. *Journal of Atmospheric and Oceanic Technology*, 34(11), 2509–2532. <https://doi.org/10.1175/JTECH-D-17-0055.1>
- Poulain, P.-M., Centurioni, L., & Özgökmen, T. (2022). Comparing the currents measured by CARTHE, CODE and SVP drifters as a function of wind and wave conditions in the southwestern mediterranean sea. *Sensors*, 22(1), 353. <https://doi.org/10.3390/s22010353>
- Sterl, A., & Caires, S. (2005). Climatology, variability and extrema of ocean waves: The web-based KNMI/ERA-40 wave atlas. *International Journal of Climatology*, 25(7), 963–977. <https://doi.org/10.1002/joc.1175>